PCCP

Interlayer spacing in pillared and grafted MCM-22 type silicas: Density functional theory analysis versus experiment

SCHOLARONE™
Manuscripts

Interlayer spacing in pillared and grafted MCM-22 type silicas: Density functional theory analysis versus experiment†

Yong Han,*[a,b] Puranjan Chatterjee,[a,c] Sardar B. Alam,[a] Tanya Prozorov,[a] Igor I. Slowing[a,c] and James W. Evans[a,b]

Pillaring of synthetic layered crystalline silicates and aluminosilicates provides a strategy to enhance their adsorption and separation performance, and can facilitate the understanding of such behavior in more complex natural clays. We perform the first-principles density functional theory calculations for the pillaring of the *pure silica polymorph* of an MCM-22 type molecular sieve. Starting with a precursor material MCM-22P with fully hydroxylated layers, a pillaring agent, $(EtO)_3SiR$, can react with hydroxyl groups $(-OH)$ on adjacent internal surfaces, $2(-OH) + (EtO)_3SiR + H_2O \rightarrow (-O)_2SiOHR + 3EtOH$, to form a pillar bridging these surfaces, or with a single hydroxyl, $-OH + (EtO)_3SiR + 2H_2O \rightarrow (-O)Si(OH)_2R + 3EtOH$, grafting to one surface. For computational efficiency, we replace the experimental organic ligand, R, by a methyl group. We find that the interlayer spacing in MCM-22 is reduced by 2.66 Å relative to weakly bound layers in the precursor MCM-22P. Including $(-O)_2SiR$ bridges for 50% (100%) of the hydroxyl sites in MCM-22P increases the interlayer spacing relative to MCM-22 by 2.52 Å (2.46 Å). For comparison, we also analyze the system where all $-OH$ groups in MCM-22P are replaced by non-bridging grafted $(-O)Si(OH)_2R$ which results in a smaller interlayer spacing expansion of 2.17 Å relative to MCM-22. Our results for the interlayer spacing in the pillared materials are compatible with experimental observations for a similar MCM-22 type material with low Al content (Si:Al = 51:1) of an expansion relative to MCM-22 of roughly 2.8 Å and 2.5 Å from our x-ray diffraction and scanning transmission electron microscopy analyses, respectively. The analysis latter reveals significant variation in individual layer spacings.

[a] Division of Chemical and Biological Sciences, Ames National Laboratory, Ames, Iowa 50011, USA.
[b] Department of Physics and Astronomy, Iowa State University, Ames, Iowa 50011, USA.
[c] Department of Chemistry, Iowa State University, Ames, Iowa 50011, USA.

* Corresponding author email: y27h@ameslab.gov

ORCID iDs:

Yong Han https://orcid.org/0000-0001-5404-0911
Puranjan Chatterjee https://orcid.org/0000-0001-8107-4498
Sardar B. Alam https://orcid.org/0000-0002-3906-2837
Tanya Prozorov https://orcid.org/0000-0001-7792-4103
Igor I. Slowing https://orcid.org/0000-0002-9319-8639
James W. Evans https://orcid.org/0000-0002-5806-3720

1. Introduction

There is currently intense interest in two-dimensional (2D) or layered materials, and furthermore in the manipulation of these materials to optimize properties. This includes numerous investigations of multilayer graphene or graphite, of transition metal dichalcogenides, and of more complex heterogeneous or hybrid structures [1, 2, 3, 4, 5]. Often, properties are changed by physical doping or intercalation of metal or other atoms [6, 7, 8, 9, 10, 11]. Another class of layered materials involves aluminosilicates. Again, for these materials, there is interest in manipulating structure and properties, which for these systems can be achieved by chemical reaction with a pillaring agent.

Molecular sieves are crystalline microporous materials [12, 13] with pore sizes which can accommodate the adsorption of some molecular species. This property facilitates diverse applications of molecular sieves in industry for adsorption and chemical separations, catalysis, water purification, etc. [14, 15, 16]. Significantly, natural layered minerals such as kaolinite and halloysite are known to preferentially adsorb heavy rare earth elements (REE) [17, 18]. However, fundamental analysis of behavior in such complex systems is challenging. This prompts development and analysis of synthetic crystalline layered aluminosilicates with selective uptake of desired elements such as REE, thereby providing a class of well-defined materials which facilitates the determination of structure-activity relationships.

In addition, a capability for predictive tuning of interlayer spacing in this class of synthetic materials provides a key strategy for controlling interactions of adsorbed and intercalated metals and/or metal oxides needed for selective separations, e.g., of REE from diverse feedstocks. One can modify the interlayer spacing (both the periodicity of the material orthogonal to the layers and the gap between the layers), as well as internal surface chemistry of such systems by incorporating chelators as pillaring agents, i.e., moieties that bridge neighboring layers. Pillaring can potentially improve stability of the layered materials against delamination, e.g., during repeated adsorption-desorption cycles. In addition, the chelators can be selected to have high binding capacity and specificity towards desired elements, e.g., REE.

We plan to use MCM-22 type materials as the synthetic platform for studies of the type described above. A MCM-22 molecular sieve [14] was first synthesized as an aluminosilicate or borosilicate by Rubin and Chu [19]. MCM-22 is an abbreviation for "Mobil Composition of Matter with sequence number twenty-two". These materials also fall within a framework type designated as "MWW" in the International Zeolite Association (IZA) database code list. The hexagonal crystal structure (space group $P6/mmm$) for MCM-22 type materials was initially determined through experimental analysis by Leonowicz, et $al.$ for a calcined sample, $H_{0.033}Na_{0.043}(Al_{0.005}B_{0.071}Si_{0.924})O_2$ [14]. Later, a pure silica polymorph, originally called ITQ-1 (with the formula of SiO_2), was synthesized [20, 21] and characterized as having an MCM-22 type structure with the unit cell parameters $a = 14.21$ Å and $c = 24.95$ Å [22]. Because the unit cell of ITQ-1 version of MCM-22 includes 72 Si atoms and 144 O atoms, this silica polymorph is often denoted as $Si_{72}O_{144}$.

Experimentally, there exist several previous studies on pillaring of MCM-22 type materials. Maheshwari, *et al.* explored how to ameliorate the impact of swelling associated with pillaring on the degradation of crystal morphology along with partial loss of crystallinity [23]. Wojtaszek-Gurdak, *et al.* explored the impact of pillaring on the dispersion of noble metals and their catalytic activity [24]. From a theoretical perspective, it is appropriate to note that a cluster model analysis based on density functional theory (DFT) was applied to MCM-22 type materials to investigate isomorphic substitution [25, 26], proton hopping [27], and the distribution of acid sites [28, 29].

In this work, we use a plane-wave DFT method to explore for the first time the crystalline structure of the pure silica ITQ-1 polymorph of MCM-22 type materials, their pillared derivatives, as well as the bonding properties between the pillaring agents and the interior surfaces. The type and added amount of a pillaring agent will naturally determine the structure feature of a pillared MCM-22 type material, in particular the degree of swelling or shrinking of the interlayer spaces. Our specific analysis is motivated by recent experiments on the synthesis and analysis of an MCM-22 material for which the bidentate ligand succinic acid is used as a pillaring agent. These studies are briefly described in Section 2.2. The composition of samples in the experimental work corresponds to a Si:Al ratio of 51:1. However, we anticipate that such a low concentration of Al would not have a significant effect on interlayer spacing. Strong support for this claim is provided in the Electronic Supplementary Information Section 1 (ESI1†). Thus, as indicated above, we just consider the pure silica polymorph ITQ-1 in our DFT analysis below.

For the above-proposed organofunctional alkoxysilanes as the pillaring agents in MCM-22, the molecular geometries are generally complicated, and therefore the computational requirement for analysis incorporating these is demanding. In the experiments described above, a pillaring agent of the form $(EtO)_3SiR$ is used to react with hydroxyl groups on adjacent internal surfaces by $2(-OH) + (EtO)_3SiR + H_2O \rightarrow (-O)_2SiOHR + 3EtOH$ to bridge these surfaces. For computational viability, the more complicated experimental organic ligand, R, which corresponds to a propylsuccinic anhydride group, is replaced by a simpler methyl group ($-CH_3$). Neglecting the long chain, which moves freely in the interlayer space, is not expected to significantly impact the interlayer spacing. Analysis supporting this claim by comparing behavior for R = $-CH_3$ and R = $-CH_2CH_3$ is provided in Section ESI2†. Another possibility is that the pillaring agent reacts with only a single surface hydroxyl by $-OH + (EtO)_3SiR + 2H_2O \rightarrow (-O)Si(OH)_2R + 3EtOH$, to form a non-bridging grafted configuration binding to one internal surface. Consequently, we also consider this case (again replacing R by $-CH_3$). DFT results for interlayer spacing in the pillared or grafted materials are compared with DFT results for bulk MCM-22, and for the pure silica precursor MCM-22P with Si:Al = 1:0, as well with experimental measurements for a similar MCM-22 material with Si:Al = 51:1.

In Section 2, we review methodology used in this paper, in particular for the DFT analysis which is the main component of this study. In addition, we describe key aspects of a complementary experimental study of MCM-22 materials, focusing on results for the

interlayer spacing. In Section 3, we present DFT results for structure and specifically for interlayer spacing of MCM-22 materials with various degrees of pillaring. In Section 4, we present DFT results for the case where the pillaring agent grafts only to a single interior surface rather than forming pillars connecting adjacent surfaces. Additional analysis of bonding in the interlayer regions is presented in Section 5, and further discussion and conclusions is provided in Section 6.

2. Theoretical methodology and experimental analysis

2.1. DFT Methodology

Several previous DFT-based analyses on MCM-22 type materials were based on non-periodic cluster models [25, 26, 27, 28, 29], for which the B3LYP hybrid functionals were used. However, such a method is very demanding for larger systems considered in this work. We note that there have been a series of comparisons between non-periodic cluster calculations and periodic calculations, e.g., for adsorption of NH_3 and H_2O molecules in acidic chabazite, where the B3LYP-level results from the cluster calculations support the reliability of periodic calculations [30]. In addition, we also note early first-principles periodical study on adsorption properties of linear hydrocarbons in zeolites within both local-density and generalized-gradient approaches [31], as well as a recent study on complex processes in a two-dimensional (2D) layered zeolite such as biomass conversion catalysis [32]. In both cases, the Vienna *Ab Initio* Simulation Package (VASP) code [33] with a plane wave basis set was implemented with Perdue-Burke-Ernzerhof (PBE) generalized-gradient approximation (GGA) [34].

Considering the above information from previous studies and also considering computational efficiency, in this study, we use the VASP code to perform all first-principles DFT calculations with the projector-augmented-wave pseudopotentials [35] developed by the VASP group. The electron-electron exchange correlation component is chosen to be the optB88-vdW functional [36], which includes the van der Walls (vdW) interactions. This functional has already been proven very successful when applied for various vdW materials [36, 37, 38, 39, 40, 41]. As an aside, this same functional is also effective in treating various small molecules consisting of C, H, O and N [42] which is important for analysis of the intercalation of such moieties in vdW materials. As a benchmark analysis, we successfully used this DFT method to calculate the bulk properties of a silica polymorph, α-quartz (see Section ESI3†). Additional benchmark analysis on small molecule geometries related to pillaring is provided in Section ESI4†.

Here, we first present DFT predictions for the bulk properties of the pure silica polymorph of MCM-22 with Si:Al = 1:0. The unit cell for three different orientations is shown in **Figs. 1a–c**. Along the a_3 direction (i.e., [0001] direction), layers have a periodicity of c and two adjacent layers are connected by two Si-O bonds per unit cell. Two O atoms in these two Si-O bonds are denoted as O_I and O_{II}, and shown as pink-colored in **Figs. 1a–c**. Using the above DFT method, we obtain the lattice constants $a = 14.4542$ Å and $c = 25.2094$ Å, which are in good agreement with experimental values. See Section ESI5†,

4

where details of the calculation and more information about the bulk properties, including formation enthalpy and bulk modulus, are also provided.
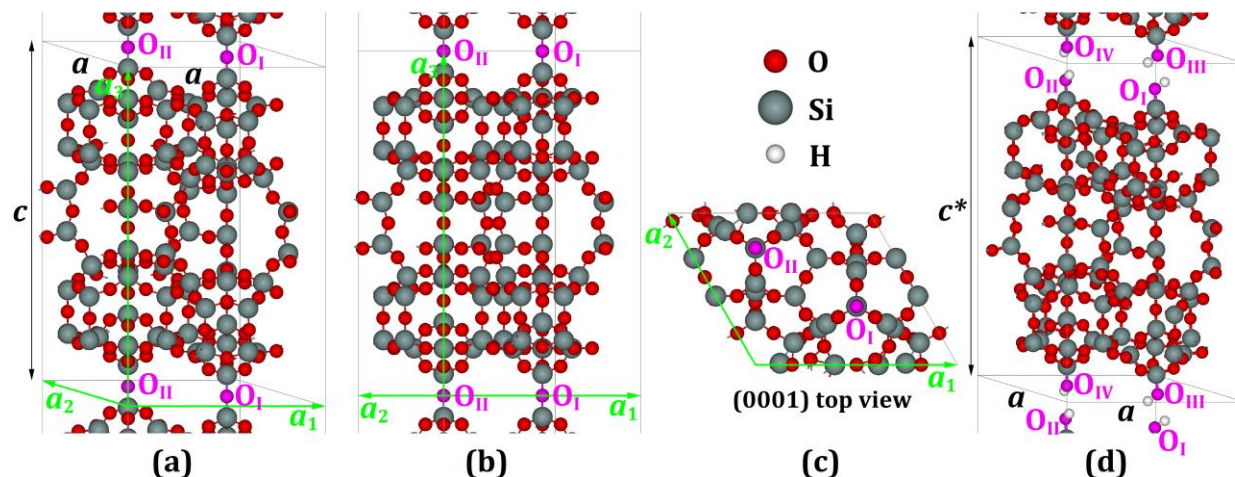

Fig. 1 (a) A 3-dimentional (3D) view, (b) a ($01\bar{1}0$) side view, and (c) a (0001) top view of the pure silica MCM-22 crystal. Three primitive vectors a_1, a_2, and a_3 of the hexagonal unit cell ($Si_{72}O_{144}$) are indicated with $|a_1| = |a_2| = a$, $|a_3| = c$, $\alpha = \beta = 90°$, and $\gamma = 120°$, where α, β, and γ are the angles between a_2 and a_3, between a_1 and a_3, and between a_1 and a_2, respectively. (d) A fully relaxed configuration at $\Delta c = c^* - c = 2.6701$ Å for the precursor MCM-22P. The types of atoms are identified by different colors of spheres.

In all DFT calculations, we select the energy cutoff to be 600 eV. The supercell sizes and corresponding k meshes including the k-point test information are also provided in Section ESI5†. All atoms in the supercell are fully relaxed. The convergence criterion of total energy is that the force exerted on each relaxed atom is less than 0.01 eV/Å.

2.2. Experimental Analysis

MCM-22 was prepared from a layered precursor (MCM-22P) synthesized via a static method following a procedure detailed in the literature [43]. The amount of Si and Al in the material can be controlled during the initial synthesis of the precursor by adjusting the sodium aluminate content in the mixture keeping all other reagents same. Briefly, to prepare MCM-22 with Si:Al = 51:1 ratio, 12.9 mmol (0.516 g) sodium hydroxide was added to a mixture of 2.22 mol (40 g) of H_2O and 2.54 mmol (0.208 g) sodium aluminate and stirred. To this mixture, ca. 98.9 mmol (7.72 g) silicic acid and ca. 39.5 mmol (4.46 mL) hexamethyleneimine was added. The mixture was then stirred at 500 rpm for 30 min and transferred to an autoclave for aging at 45 °C for 24 h. After that, the autoclave was kept in an oven for 9 d at 150 °C. The material was then filtered by washing thoroughly with nanopure water and dried overnight under vacuum to obtain the MCM-22P. The material was then calcined at 550 °C for 10 h to obtain MCM-22. As an aside, we note that to instead prepare a material with Si:Al = 20:1 and 42:1 ratio, 1.04 g and 0.460 g $NaAlO_2$ would be added, respectively. The materials were characterized using powder x-ray diffraction (XRD). The Al content of the materials was determined by inductively coupled plasma - optical emission spectroscopy (ICP-OES).

Our MCM-22P with a low aluminum content (a Si:Al ratio of 51:1) was swollen with cetyltrimethyl ammonium bromide (CTAB) and reacted for 48 h with 3-(triethoxysilyl)propylsuccinic anhydride (SA-TES). More specifically, 0.5 g MCM-22P was mixed with ca. 1.0 g tetrapropyl ammonium hydroxide (TPA-OH) (40%) and 4.0 g of CTAB and 10.0 g water was added to the mixture. The mixture was then stirred at room temperature for 18 h. After that, the solid was filtered and washed with water and dried in vacuum. Total weight of the swelled material was ca. 2.5 g. Then, 1.5 g of the swelled material was mixed with 1.5 mL (3-triethoxylsilyl)propyl succinic anhydride and ca. 100 mL toluene. The mixture was stirred at 100 °C for 24 h. The functionalized material was then filtered and washed thoroughly with H_2O and ethanol and dried overnight under vacuum to obtain SA-MCM-22. See Section ESI6† for further details.

MCM-22P generally has pending silanol (Si–OH) and aluminol (Al–OH) groups on the interlayer surfaces. Calcination of MCM-22P leads to condensation of silanol groups between neighboring layers to produce the microporous MCM-22 with decreased interlayer spacing. Alternatively, reaction with bifunctional compounds that condense with the interlayer silanols can result in formation of pillars between layers, and retention or even an increase of the interlayer spacing. As indicated above, triethoxysilyl derivatized succinic anhydride (SA) group was used as a pillaring agent.

The XRD patterns for the material after addition of the pillaring agent (designated as SA-MCM-22) indicate a shift in the reflections of the (002), (100) and (101) peaks towards smaller angles compared to the calcined MCM-22 material (see Section ESI6†). Specifically, our XRD analysis indicates d-spacings measuring periodicity orthogonal to the layers of 27.4 Å for MCM-22P, 25.3 Å for MCM-22, and 28.1 Å for SA-MCM-22. This implies a shift of ca. 2.8 ±0.1 Å in d-spacing [based on the (100) peak] for SA-MCM-22 with a d-spacing above that of the calcined material, MCM-22. Analysis via Fourier transform infrared (FTIR) spectroscopy confirms the presence of the pillaring agent in the resulting material (see Section ESI6†).

Images of this MCM-22 material with Si:Al = 51:1, both with and without addition of the pillaring agent, were also acquired by scanning transmission electron microscopy in high-angle annular dark-field mode (HAADF-STEM) with an aberration-corrected Thermo Scientific Titan Themis Cubed operating at 200 kV. Images were recorded with the Cs-corrected probe, using the spot size 9, with an e-beam current of 15 pA. **Fig. 2a** shows an image of MCM-22 without the pillaring agent. Analysis of multiple images reveals an average interlayer periodicity (i.e., the unit cell dimension c along [0001] direction) of 25.5 ±0.1 Å. **Fig. 2b** shows an image of MCM-22 after addition of the pillaring agent, succinic anhydride, as in the above XRD studies. In this case, analysis of multiple images reveals that the average interlayer periodicity has increased to 28.0±0.4 Å. The associated variation in individual interlayer periodicity in a range from roughly 26 Å to 30 Å occurs not just between MCM-22 particles, but also within a single particle (see Section ESI7†). This variation likely reflects different degrees of pillaring in different interlayer spaces, in addition to possible grafting rather than pillaring.
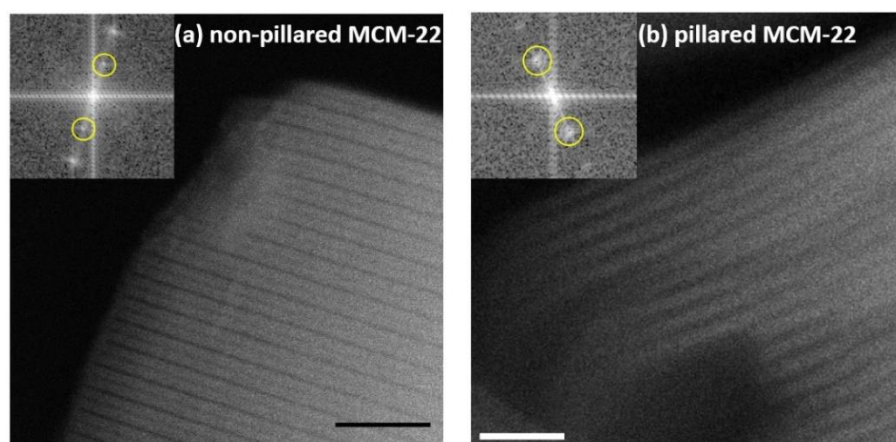
Fig. 2. HAADF-STEM image of MCM-22 with Si:Al = 51:1 (a) without pillaring, and (b) with pillaring using succinic anhydride. A fast Fourier transform of the image is shown in the insets where the spots associated with interlayer periodicity are marked by yellow circles, and these are utilized to determine average periodicities cited in the text. The scale bars are 10 nm.

3. DFT results for MCM-22P (no pillaring) and for MCM-22 with pillaring

DFT analysis is performed for MCM-22 with various degrees of pillaring, and for MCM-22P which might be regarded as the limiting case of no pillaring. Consistent with Section 2.1, analysis is performed for the *pure silica polymorph*. The pillaring reaction involves a pair of surface hydroxyls on adjacent surfaces and is described by $2(-OH) + (EtO)_3SiR + H_2O \rightarrow (-O)_2SiOHR + 3EtOH$, replacing R by CH_3, as noted in Section 1. Behavior is expected to vary little from that for the material with low Al content Si:Al = 51:1 for which experimental analysis was described in Section 2.2. Further discussion and evidence for this claim is provided in ESI1†.

The subsections below report results for a natural sequence of cases. First, Section 3.1 considers MCM-22P which corresponds to the complete absence of pillaring. Here, groups on the interior surfaces are 100% −OH with 0% pillared. Then, Section 3.2 considers the case of partial pillaring with 50% of surface groups remaining as −OH, and 50% converted to the pillaring or bridging unit $(-O_2)SiOHCH_3$. Finally, Section 3.3 considers the case of complete pillaring with 0% of surface groups remaining as −OH and 100% converted to $(-O_2)SiOHCH_3$.

3.1. MCM-22P without pillaring: 100% −OH + 0% $(-O_2)SiOHCH_3$

We first analyze the pure silica precursor MCM-22P with fully hydroxylated internal surfaces. Relative to pure silica MCM-22, the two O atoms (O_I and O_{II} in **Figs. 1a–c**) connecting adjacent layers are replaced with four hydroxyl groups, O_IH, $O_{II}H$, $O_{III}H$, and $O_{IV}H$ per unit cell, as shown in **Fig. 1d**.

To obtain the energetically most favorable structure of MCM-22P, we perform a series of calculations by varying the unit cell dimension c^* (see **Fig. 1d**) which corresponds to the experimental d-spacing along the [0001] direction but leaving other two dimensions a to be the same as those for the bulk in **Fig. 1a**. The total energy of the supercell versus the unit cell dimension change $\Delta c = c^* - c$ (relative to the pure silica MCM-22 bulk unit cell dimension $c = 25.2094$ Å from our DFT calculation) along the [0001] direction is plotted in **Fig. 3a**, and an energy minimum is found at $\Delta c = 2.66$ Å, which is obtained by interpolating the DFT data points around this value. The result of $\Delta c = c^* - c = 2.66$ Å indicates that the precursor MCM-22P is swollen significantly relative to the MCM-22 bulk structure along the [0001] direction.
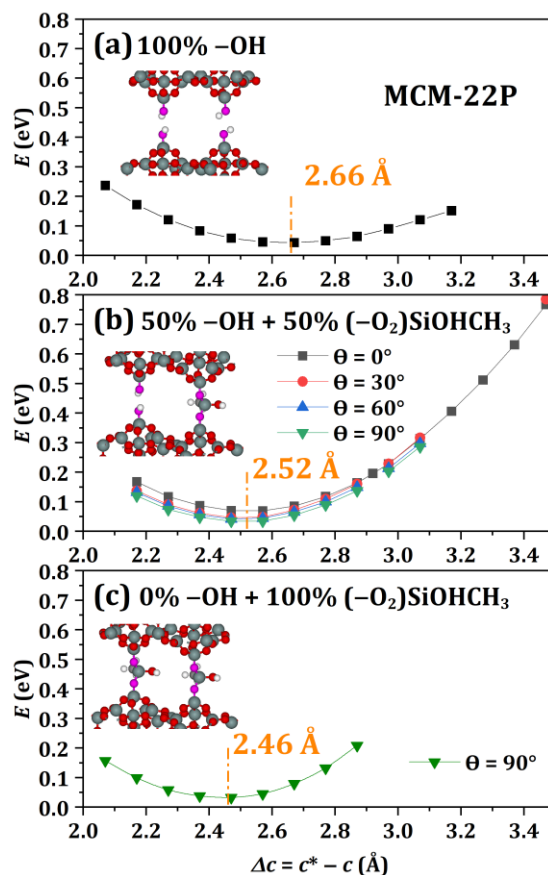

Fig. 3 Total energies versus $\Delta c = c^* - c$, the change of unit cell size along the [0001] direction for (a) 100% −OH, i.e., pure silica MCM-22P, (b) 50% −OH + 50% (−O$_2$)SiOHCH$_3$, and (c) 0% −OH + 100% (−O$_2$)SiOHCH$_3$. The insets indicate the corresponding structures.

In the above calculations for the precursor, the supercell is always taken to be the unit cell in **Fig. 1d**. In addition, for any given c^*, we find that the positions of four H atoms undergo significant relaxation relative to their initial positions. This indicates that the results are most likely independent of their initial positions, although multiple local energy minima cannot be completely ruled out. A comprehensive search for local energy minima

8

using many initial configurations incurs considerable computational expense, and is therefore not performed in this work. We expect that different local energy minima, if they exist, are not significantly different. This scenario is realized in the following analysis of pillared MCM-22 for which even taking different initial configurations of the pillaring species does not significantly change total energies.

3.2. MCM-22 with partial pillaring: 50% −OH + 50% (−O₂)SiOHCH₃

In this section, starting from pure silica MCM-22P, we remove the two H atoms from the pair of hydroxyl groups, O_IH and $O_{III}H$, and add the pillaring group $=SiOHCH_3$ bonded to both O_I and O_{III}. This pillaring group might be regarded as deriving from trimethylsilanol after removing two methyl groups (see **Fig. 4a**).
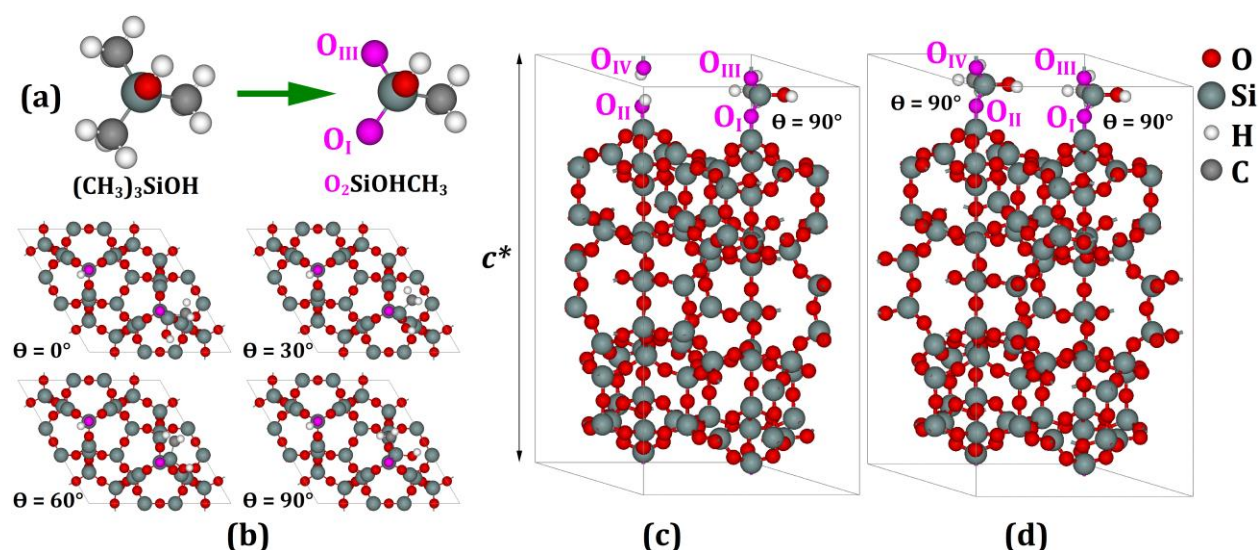

Fig. 4 (a) The initial pillared configuration for DFT analysis can be regarded as being obtained by replacing 2 methyl groups in a trimethylsilanol molecule $(CH_3)_3SiOH$ with the two O atoms (O_I and O_{III}). (b) The (0001) top views of four initial configurations for 50% −OH + 50% (−O₂)SiOHCH₃ in our DFT calculations with four different initial orientations (azimuths $\theta = 0°, 30°, 60°$, and $90°$) of $=SiOHCH_3$. (c) A fully relaxed configuration at $\Delta c = c^* - c = 2.4701$ Å for 50% −OH + 50% (−O₂)SiOHCH₃ with initial $\theta = 90°$ for one $SiOHCH_3$ group per unit cell. (d) A fully relaxed configuration at $\Delta c = c^* - c = 2.4701$ Å for 0% −OH + 100% (−O₂)SiOHCH₃ with initial $\theta = 90°$ for two $=SiOHCH_3$ groups per unit cell.

After adding the agent $=SiOHCH_3$ into the space between layers and fully relaxing the system, the total energy may depend on the initial configuration of the agent if there are multiple local energy minima. Again, definitive determination of the global energy minimum starting with many initial configurations is computationally demanding and therefore not performed in this work. Instead, we only consider four initial orientations of an added $=SiCH_3OH$. The orientation is simply characterized by an azimuth θ around the axis O_I-O_{III}, as illustrated in **Figs. 4b–c**. The four initial orientations of $=SiCH_3OH$ on the O_I-

O_{III} axis are taken to be $\theta = 0°, 30°, 60°$, and $90°$, shown in **Fig. 4b**. These four initial orientations are expected to be sufficient to determine the global energy minimum after considering the symmetry of the system.

Similar to the calculations for MCM-22P in Section 3.1, we perform a series of calculations by varying the unit cell dimension c^* for each initial orientation of the added =SiCH₃OH. The total energy versus $\Delta c = c^* - c$ are plotted in **Fig. 3b**, where the curves for the four initial θ are close to each other around their energy minima, and so the corresponding four energy minima are effectively identical. By interpolating the DFT data points on the lowest curve for $\theta = 90°$ in **Fig. 3b**, we find $\Delta c = 2.52$ Å at its energy minimum, close to which a fully relaxed configuration is illustrated as **Fig. 4c**. The Δc value of 2.52 Å for 50% −OH + 50% (−O₂)SiOHCH₃ is slightly smaller than $\Delta c = 2.66$ Å for the precursor.

3.3. MCM-22 with complete pillaring: 0% −OH + 100% (−O₂)SiOHCH₃

Each unit cell of pure silica MCM-22P includes two equivalent interlayer upper-lower OH pairs (O_IH-O_{III}H and O_{II}H-O_{IV}H) (see **Fig. 1d**). In this section, we remove all four H atoms from both pairs of hydroxyl groups in MCM-22P and add one pillaring group =SiOHCH₃ bonded to O_I and O_{III}, and another to O_{II} and O_{IV}. The analysis for 50% OH + 50% (−O₂)SiOHCH₃ in Section 3.2 indicates that the initial orientations of the added =SiOHCH₃ do not significantly affect the optimized energies. Thus, we only consider one type of initial orientation of two =SiOHCH₃ groups in a unit cell for 0% OH + 100% (−O₂)SiOHCH₃. We choose $\theta = 90°$ for both =SiOHCH₃ groups, as illustrated in **Fig. 4d**.

After a series of calculations by varying the unit cell dimension c^*, we plot the total energy versus Δc in **Fig. 3c**. By interpolating the DFT data points, we find $\Delta c = 2.46$ Å at the energy minimum. As an illustration, **Fig. 4d** is a fully relaxed configuration close to the energy minimum of the curve in **Fig. 3c**. The Δc value of 2.46 Å for 0% −OH + 100% (−O₂)SiOHCH₃ is slightly smaller than $\Delta c = 2.52$ Å for 50% −OH + 50% (−O₂)SiOHCH₃ and $\Delta c = 2.66$ Å for the precursor (100% −OH).

4. DFT analysis of grafted configurations incorporating the pillaring agent

As noted in Section 1, it is possible that the pillaring agent reacts with and binds or grafts to only a single surface hydroxyl, −OH + (EtO)₃SiR + 2H₂O → (−O)Si(OH)₂R + 3EtOH, where again we replace R by CH₃, to form a non-pillared (non-bridging) grafted configuration. Consequently, a large number of configurations are possible in the presence of pillaring agent which include various combinations of both bridging (or pillared) configurations and non-pillared (or non-bridging) grafted configurations. As a benchmark calculation, we consider only the extreme case where only non-bridging grafted groups, (−O)Si(OH)₂R′ with R′ = CH₃, are present, and where grafting such has occurred with 100% of surface silanol groups (see **Fig. 5**). We emphasize that any analysis with multiple non-

bridging groups is challenging given the large number of possible configurations, i.e., distinct orientations, which these can adopt.

For the systems with 0% −OH + 100% (−O)Si(OH)$_2$CH$_3$ considered here, one expects that the initial configurations of the (−O)Si(OH)$_2$CH$_3$ might significantly affect the final fully relaxed structures and the corresponding energies. In Sections 3.2 and 3.3, the bridging =SiCH$_3$OH group is pinned by a vertical O$_I$-Si-O$_{III}$ (or O$_{II}$-Si-O$_{IV}$) bridge, and therefore the orientation of =SiCH$_3$OH is determined only by a single azimuth θ. However, the non-bridging grafted (−O)Si(OH)$_2$CH$_3$ considered in this section is pinned by only one O$_{I, II, III, or IV}$-Si bond, and its orientation is determined by both an azimuth θ and an altitude φ. Analogous to the simpler case of a bridging species in Sections 3.2 and 3.3, to search the global energy minimum for a given c^*, one can, in principle, relax the configurations by taking as many initial choices of θ and φ as possible. Naturally, this approach is extremely computationally demanding particularly with DFT-level energetics.
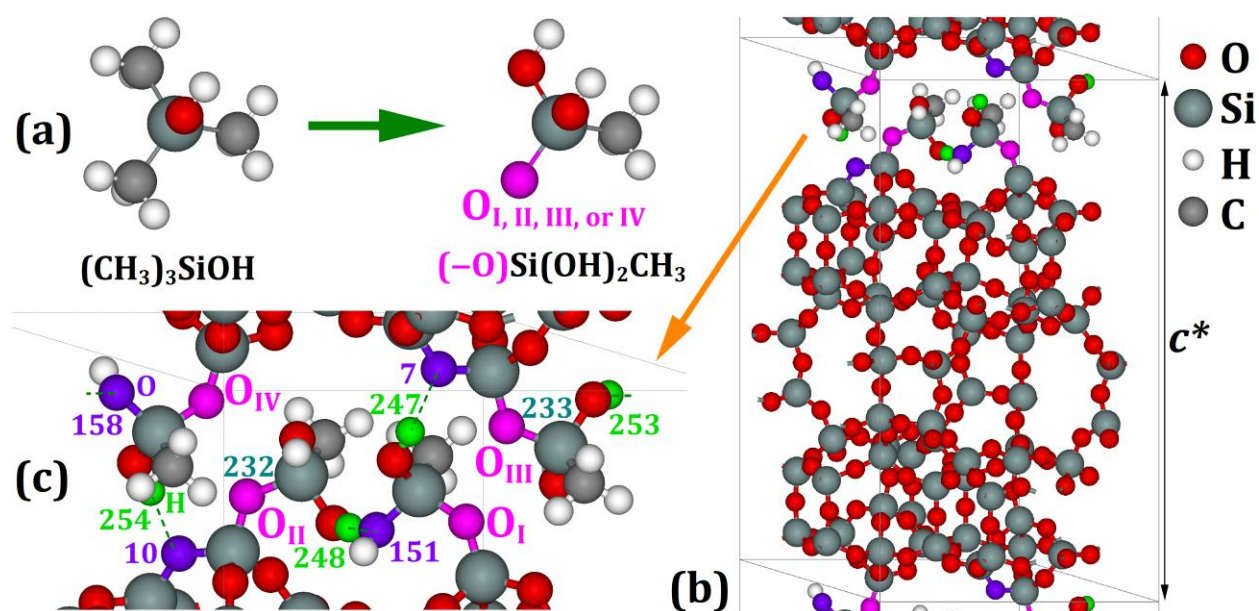

Fig. 5 (a) The initial grafted configuration for DFT analysis can be regarded as being obtained by replacing one methyl group in a trimethylsilanol molecule (CH$_3$)$_3$SiOH with one O atom (O$_I$, O$_{II}$, O$_{III}$, or O$_{IV}$) and another with a hydroxyl group OH. (b) A fully relaxed configuration with 100% (−O)Si(OH)$_2$CH$_3$ at $\Delta c = c^* - c = 2.2103$ Å. (c) Local enlargement of (b), showing the details of bonding between the pillaring agent to the upper and lower layers. The H-bonds are indicated by the olive dashed lines. One green ball and one purple ball with the same-colored identification (ID) numbers are connected by an olive dashed line, indicating the formation of a H-bond.

Thus, we consider below another approach which includes a stochastic (random) choice of initial orientations for the grafted species followed by molecular dynamics (MD) simulation at appropriate temperatures with a fixed c^*. Finally, energy minimization is implemented to obtain a fully relaxed configuration. Due to the random initial

configurations, the final relaxed configurations from N trials produce up to N local energy minima (noting that some may coincide). Then, the lowest of these should be close to the global energy minimum (at least for sufficiently large N). In principle, the above analysis can be based upon *ab initio* molecular dynamics (AIMD). However, AIMD simulations have a very high computational cost for our system with more than 200 atoms. Thus, we implement the MD simulations based upon an empirical force field (FF). See Section ESI8† for details of the MD simulations. From a series of tests by using QuantumATK MD software [44], we find that the ReaxFF of van Duin *et al.* [45, 46] satisfies our requirements. We do note that the parameterization from Psofogiannakis *et al.* [45] was focused on the treatment of elements Si, Al, O, and H rather than C. However, we emphasize that any limitations in FF reliability are not so deleterious as the configurations produced by FF MD are finally reoptimized with the DFT method.
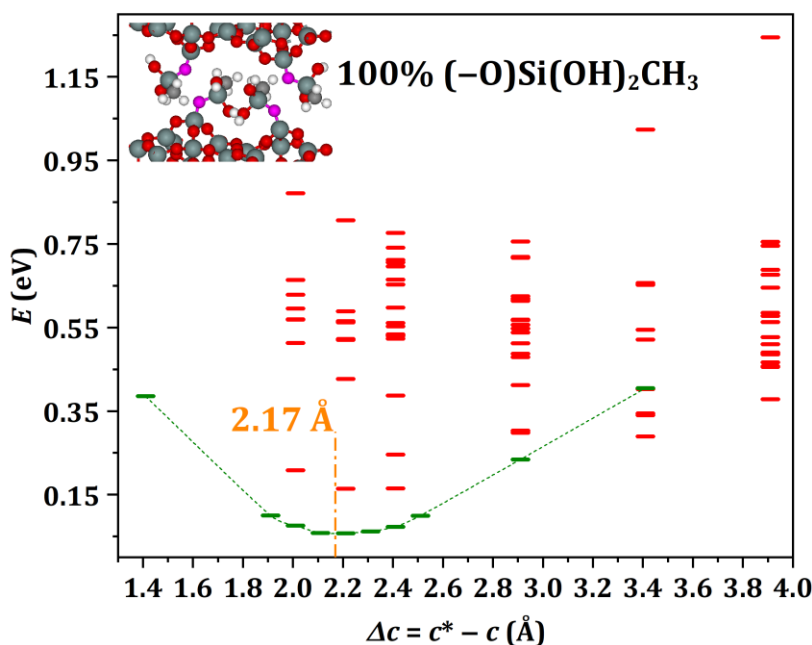

Fig. 6 Total energies (local energy minima) versus Δc for 0% −OH + 100% (−O)Si(OH)$_2$CH$_3$. The inset indicates a fully relaxed structure showing an interlayer space region with 100% (−O)Si(OH)$_2$CH$_3$.

   Fig. 6 shows local energy minima results from the FF MD-based approach as red bars, where we obtain multiple ($N = 9$ or 18) such minima for six c^* values. At $\Delta c = 2.9103$ Å, the local energy minimum from this approach with the lowest energy is relabeled as a green bar in **Fig. 6**. We then use the optimized configuration corresponding to this green bar at $\Delta c = 2.9103$ Å as the initial configurations to perform full relaxations for other nine c^* values, also marked as 9 green bars in **Fig. 6**. Around $\Delta c \approx 2.2$ Å, each green bar is lower than all red bars for any given c^*, so these configurations likely correspond to the global energy minima. This is not necessarily the case for other Δc as is evident from results at $\Delta c = 3.4103$ Å. By interpolating energies from the green bars around $\Delta c \approx 2.2$ Å (the dotted curve in **Fig. 6**), we obtain $\Delta c = 2.17$ Å at its global energy minimum. This is close to

the fully relaxed configuration is illustrated in **Fig. 5b**. The Δc value of 2.17 Å is smaller than the values of $\Delta c = 2.46$ to 2.66 Å for the precursor and for the pillared configurations analyzed in Section 3. See Section 5 for related discussion.

5. Atomic bonding properties in the interlayer regions

For systems with pillaring, the covalent bonding in the −O−Si−O− bridging unit is naturally a key factor controlling the interlayer spacing. However, for partial pillaring, hydrogen bonding (H-bonding) between layers is also relevant. For the precursor, MCM-22P, one expects that H-bonding plays a dominant role in determining interlayer spacing. The same is true for the non-pillared grafted structure considered in Section 4, noting that the pillaring agents contain a substantial proportion of H atoms.

H-bonds, denoted as X−H···A, primarily involve electrostatic attraction between a H atom (covalently bound to a more electronegative atom or group X) and another electronegative atom A [47], where, in our systems, X = A = O. To judge whether a H-bond is strong (S), medium (M), or weak (W) from its geometric parameters, one can utilize the Jeffrey's classification based upon H···A separations, $s_{H···A}$, as suggested by Steiner [47]. One assigns $s_{H···A}$ from 1.2 to 1.5 Å as S, from 1.5 to 2.2 Å as M, and > 2.2 Å as W (see Section ESI9†). We emphasize that there are no stringent borderlines between S, M, and W. Type M resembles H-bonds between water molecules or in carbohydrates, and therefore can be also called the normal H-bonds [47, 48]. If $s_{H···O} > 2.3$ Å in our systems, the bonds are weak and vdW-like, and are not considered as H-bonds in this study. In **Table 1**, we list all H-bonds with $s_{H···O} < 2.3$ Å for the fully relaxed configurations in **Figs. 1, 4, and 5**.

Table 1. Bond lengths and bond angles of 10 strongest H-bonds in the configurations in **Figs. 1, 4, and 5**. The numbers in the first column denote the ID of the corresponding atoms (see Section ESI10†). The bold fonts indicate two stronger key H-bonds binding the upper and lower layers in the configuration of **Fig. 5b or 5c**.

H-bond	Configuration	$s_{H···O}$	s_{OO}	$s_{O−H}$	$\phi_{O−H···O}$
O146−H219···O2	Fig. 1d	2.278	2.763	0.971	109.8
O2−H220···O146	Fig. 1d	2.267	2.763	0.971	110.6
O145−H221···O1	Fig. 1d	2.288	2.761	0.971	108.9
O1−H222···O145	Fig. 1d	2.259	2.761	0.971	111.1
O147−H226···O3	Fig. 4c	2.167	2.643	0.972	108.6
O3−H227···O147	Fig. 4c	2.125	2.643	0.972	111.6
O155−H247···O7	Fig. 5b or 5c	**1.953**	**2.915**	**0.976**	**168.4**
O156−H248···O151	Fig. 5b or 5c	1.784	2.767	0.986	174.7
O153−H253···O158	Fig. 5b or 5c	1.784	2.767	0.986	174.5
O154−H254···O10	Fig. 5b or 5c	**1.952**	**2.914**	**0.976**	**168.4**

For the configuration of the precursor in **Fig. 1d**, four H-bonds involving upper and lower layer hydroxyl groups are found: O146–H219⋯O2, O2–H220⋯O146, O145–H221⋯O1, and O1–H222⋯O145 (for definitions of these ID numbers, see Section ESI10†), with 2.2 Å $< s_{H⋯O} <$ 2.3 Å, $s_{OO} = 2.643$ Å, $s_{O-H} = 0.972$ Å, and $\phi_{O-H⋯O} \approx 110°$, which are close to the borderline between W and M type. For the partially pillared configuration 50% –OH + 50% (–O$_2$)SiOHCH$_3$ in **Fig. 4c**, two H-bonds again involving upper and lower layer hydroxyl groups are found: O147–H226⋯O3 and O3–H227⋯O147, with 2.1 Å $< s_{H⋯O} <$ 2.2 Å, $s_{OO} \approx 2.76$ Å, $s_{O-H} = 0.971$ Å, and $\phi_{O-H⋯O} \approx 110°$, which are between W and M type. For the completely pillared configuration 0% OH + 100% (–O$_2$)SiOHCH$_3$ in **Fig. 4d**, H-bonding is not so relevant.

For the non-pillared grafted configuration of 0% –OH + 100% (–O$_2$)SiOHCH$_3$ in **Fig. 5b**, we find four H-bonds: O155–H247⋯O7 and O154–H254⋯O10 (highlighted by bold fonts in **Table 1**), with $s_{H⋯O} \approx 1.95$ Å, $s_{OO} \approx 2.91$ Å, $s_{O-H} = 0.976$ Å, and $\phi_{O-H⋯O} \approx 168°$; O156–H248⋯O151 and O153–H253⋯O158, with $s_{H⋯O} = 1.784$ Å, $s_{OO} = 2.767$ Å, $s_{O-H} = 0.986$ Å, and $\phi_{O-H⋯O} \approx 175°$. The geometric parameters of all these four H-bonds correspond to stronger Type M. In **Fig. 5c**, we highlight these four H-bonds by colors for which H is green, the acceptor atom O is purple, and the donor atom O is red. Note that the periodic boundary condition is needed to be considered for the geometry of O153–H253⋯O158. For further discussion, see Section ESI10†. In summary, only weaker H-bonds are found in the interlayer regions for the precursor and for partially pillared configurations. In contrast, for the non-pillared grafted configuration, the stronger H-bonds between pillaring agents grafted to the upper and lower surfaces likely produce the significant reduction in interlayer spacing relative to the precursor.

6. Discussion and conclusions

Our DFT analysis explores the increase in interlayer spacing relative to the pure silica polymorph of the MCM-22 molecular sieve (ITQ-1) by adding a succinic anhydride type pillaring agent to a MCM-22 precursor. This agent can either form pillars between the upper and lower surfaces of the interlayer spaces, or it can graft to a single upper or lower surface. Relative to MCM-22, the interlayer spacing increases by $\Delta c = 2.52$ Å for partially pillared configuration, by $\Delta c = 2.46$ Å for the fully pillared configuration, and by $\Delta c = 2.17$ Å for the fully grafted configuration. These increases are similar, and furthermore the Δc values are reasonably compatible with the experimental estimates of roughly 2.8 Å and 2.5 Å for the interlayer spacing increase from our XRD and STEM studies, respectively, for a similar MCM-22 type material with low Al content (Si:Al = 51:1). Given the significant variation in the individual interlayer spacings observed in our STEM studies for samples of the precursor MCM-22P after exposure to the pillaring agent, it is more than likely that these samples include different degrees of pillaring, and that some interlayer spaces contain grafted configurations.

We also analyze the nature of the bonding in the interlayer spaces for these various configurations. Only weaker H-bonds are found in the interlayer regions for the precursor. For pillared configuration, the upper and lower layers are bound by strong covalent bridging Si-O-Si bonds (where partially pillared configurations also include some weaker H-bonds). For the non-pillared grafted configuration, the stronger H-bonds between pillaring agents grafted to the upper and lower surfaces are found, likely producing the significant reduction in interlayer spacing relative to the precursor.

Given the plausible coexistence of these different structures, it natural to assess their relative thermodynamic preference by exploiting our DFT energies (where entropy effects are ignored). To this end, we assess the energy change starting with a configuration including two unit cells of the precursor MCM-22P and four pillaring agents which can convert to either (i) two unit cells of fully pillared product, or (ii) one unit cell of fully grafted product plus one extra unchanged unit cell of the precursor. Our DFT results show that the energy of the fully pillared product for each two unit cells is 1.10 eV higher than for the mixed fully grafted product and unchanged precursor. This suggests an energetic preference for grafting. See Section ESI11† for details of this analysis. However, it should be emphasized that the actual product formed in the experiments will be strongly influenced by kinetic factors, not just by thermodynamics. These factors include not only the activation barriers for pillaring or grafting reactions, but also the transport kinetics of pillaring agent into the interlayer spaces.

Finally, we note that the methodology used in this work can be applied for analysis of pillaring or grafting for the type of MCM-22 molecular sieves considered here but with non-zero Al content (which can be treated with DFT or the ReaxFF potential used here). However, our treatment is primarily based on DFT analysis which is directly applicable to a much broader class of MCM-22 type materials, and also for different pillaring agents. Of particular interest for the type of MCM-22 materials considered here is the use of other pillaring agents such as 1,4-bis(triethoxysilyl)benzene rather than triethoxysilyl derivatized succinic anhydride, where some preliminary experimental data indicate changes in interlayer spacing due to either pillaring or grafting.

Conflicts of interest

There are no conflicts to declare.

Acknowledgments

References

[1] M. J. Allen, V. C. Tung and R. B. Kaner, *Chem. Rev.*, 2010, **110**, 132–145.

[2] M. Batzill, *Surf. Sci. Rep.*, 2012, **67**, 83–115.

[3] S. Manzeli, D. Ovchinnikov, D. Pasquier, O. V. Yazyev and A. Kis, *Nat. Rev. Mater.*, 2017, **2**, 17033.

[4] W. Choi, N. Choudhary, G. H. Han, J. Park, D. Akinwande and Y. H. Lee, *Mater. Today*, 2017, **3**, 116–130.

[5] L. Maggini and R. R. Ferreira, *J. Mater. Chem. C*, 2021, **9**, 15721–15734.

[6] R. H. Friend and A. D. Yoffe, *Adv. Phys.*, 1987, **36**, 1–94.

[7] R. A. Klemm, *Physica C*, 2015, **514**, 86–94.

[8] Y. Jung, Y. Zhou and J. J. Cha, *Inorg. Chem. Front.*, 2016, **3**, 452–463.

[9] K. Ji, J. Han, A. Hirata, T. Fujita, Y. Shen, S. Ning, P. Liu, H. Kashani, Y. Tian, Y. Ito, J. Fujita and Y. Oyama, *Nat. Commun.*, 2019, **10**, 275.

[10] A. Lii-Rosales, Y. Han, D. Jing, M. C. Tringides, S. Julien, K.-T. Wan, C.-Z. Wang, K. C. Lai, J. W. Evans and P. A. Thiel, *Nanoscale*, 2021, **13**, 1485–1506.

[11] Y. Han, D. Jing, Y. Luan, C.-J. Wang, M. Kolmer, Z. Fei, M. C. Tringides and J. W. Evans, *J. Phys. Chem. Lett.*, 2022, **13**, 6651–6656.

[12] D. W. Breck, *J. Chem. Educ.*, 1964, **41**, 678–689.

[13] J. Rouquerol, D. Avnir, C. W. Fairbridge, D. H. Everett, J. H. Haynes, N. Pernicone, J. D. F. Ramsay, K. S. W. Sing and K. K. Unger, *Pure Appl. Chem.*, 1994, **66**, 1739–1758.

[14] M. E. Leonowicz, J. A. Lawton, S. L. Lawton and M. K. Rubin, *Science*, 1994, **264**, 1910–1913.

[15] J. Han, J. Fu and R. B. Schoch, *Lab Chip*, 2008, **8**, 23–33.

[16] K. Varoon, X. Zhang, B. Elyassi, D. D. Brewer, M. Gettel, S. Kumar, J. A. Lee, S. Maheshwari, A. Mittal, C.-Y. Sung, M. Cococcioni, L. F. Francis, A. V. McCormick, K. A. Mkhoyan and M. Tsapatsis, *Science*, 2011, **334**, 72–75.

[17] M. Yang, X. Liang, L. Ma, J. Huang, H. He and J. Zhu, *Chem. Geo.*, 2019, **525**, 210–217.

[18] A. Alshameri, H. He, C. Xin, J. Zhu, W. Xinghu, R. Zhu and H. Wang, *Hydrometallurgy*, 2019, **185**, 149–161.

[19] M. K. Rubin and P. Chu, *U. S. Patent* 4954325 (1990).

[20] M. J. D. Cabañas, M. A. C. Fernandez, C. C. Martires and A. C. Canos, *U. S. Patent* 6077498 (1996).

[21] M. A. Camblor, C. Corell, A. Corma, M.-J. Díaz-Cabañas, S. Nicolopoulos, J. M. González-Calbet and M. Vallet-Regí, *Chem. Mater.*, 1996, **8**, 2415–2417.

[22] M. A. Camblor, A. Corma, M.-J. Díaz-Cabañas and C. Baerlocher, *J. Phys. Chem. B*, 1998, **102**, 44–51.

[23] S. Maheshwari, E. Jordan, S. Kumar, F. S. Bates, R. L. Penn, D. F. Shantz and M. Tsapatsis, *J. Am. Chem. Soc.*, 2008, **130**, 1507–1516.

[24] A. Wojtaszek-Gurdak, I. Sobczak, K. Grzelak, M. Ziolek, U. Hartfelder, J. A. van Bokhoven, *Mater. Res. Bull.*, 2016, **76**, 169–178.

[25] Y. Wang, D. Zhou, G. Yang, S. Miao, X. Liu and X. Bao, *J. Phys. Chem. A*, 2004, **108**, 6730–6734.

[26] A. Zheng, L. Chen, J. Yang, M. Zhang, Y. Su, Y. Yue, C. Ye and F. Deng, *J. Phys. Chem. B*, 2005, **109**, 24273–24279.

[27] Y. Wang, D. Zhou, G. Yang, X. Liu, D. Ma, D. Liang and X. Bao, *Chem. Phys. Lett.*, 2004, **388**, 363–366.

[28] D. Zhou, Y. Bao, M. Yang, N. He and G. Yang, J. Mol. Catal. A, 2006, **244**, 11–19.

[29] Y. Li, W. Guo, W. Fan, S. Yuan, J. Li, J. Wang, H. Jiao and T. Tatsumi, *J. Mol. Catal. A*, 2011, **338**, 24–32.

[30] X. Solans-Monfort, M. Sodupe, V. Branchadell, J. Sauer, R. Orlando and P. Ugliengo, *J. Phys. Chem. B*, 2005, **109**, 3539–3545.

[31] L. Benco, T. Demuth, J. Hafner, F. Hutschka and H. Toulhoat, *J. Chem. Phys.*, 2001, **114**, 6327–6334.

[32] V. J. Margarit, E. M. Gallego, C. Paris, M. Boronat, M. Moliner and A. Corma, *Green Chem.*, 2020, **22**, 5123–5131.

[33] G. Kresse and J. Furthmüller, *Phys. Rev. B*, 1996, **54**, 11169–11186.

[34] J. P. Perdew, K. Burke and M. Ernzerhof, *Phys. Rev. Lett.*, 1996, **77**, 3865–3868.
[35] G. Kresse and D. Joubert, *Phys. Rev. B*, 1999, **59**, 1758–1774.

[36] J. Klimeš, D. R. Bowler and A. Michaelides, *J. Phys. Condens. Matter*, 2010, **22**, 022201.

[37] Y. Han, K. C. Lai, A. Lii-Rosales, M. C. Tringides, J. W. Evans and P. A. Thiel, *Surf. Sci.*, 2019, **685**, 48–58.

[38] Y. Han, M. C. Tringides, J. W. Evans and P. A. Thiel, *Phys. Rev. Res.*, 2020, **2**, 013182.

[39] Y. Han, J. W. Evans and M. C. Tringides, *Appl. Phys. Lett.*, 2021, **119**, 033101.

[40] Y. Han, J. W. Evans and M. C. Tringides, *Phys. Rev. Mater.*, 2021, **5**, 074004.

[41] Y. Han, J. W. Evans and M. C. Tringides, *J. Vac. Sci. Technol. A*, 2022, **40**, 012202.

[42] Submitted to *AIP Advances* (under review).

[43] I. Güray, J. Warzywoda, N. Baç and A. Sacco, Microporous Mesoporous Mater., 1999, **31**, 241–251.

[44] S. Smidstrup, T. Markussen, P. Vancraeyveld, J. Wellendorff, J. Schneider, T. Gunst, B. Verstichel, D. Stradi, P. A. Khomyakov, U. G. Vej-Hansen, M.-E. Lee, S. T. Chill, F. Rasmussen, G. Penazzi, F. Corsetti, A. Ojanperä, K. Jensen, M. L. N. Palsgaard, U. Martinez, A. Blom, M. Brandbyge and K. Stokbro, *J. Phys. Condens. Matter*, 2020, **32**, 015901.

[45] G. M. Psofogiannakis, J. F. McCleerey, E. Jaramillo and A. C. van Duin, *J. Phys. Chem. C*, 2015, **119**, 6678–6686.

[46] A. C. T. van Duin, S. Dasgupta, F. Lorant and W. A. Goddard III, *J. Phys. Chem. A* 2001, **105**, 9396–9409.

[47] T. Steiner, *Angew. Chem. Int. Ed.*, 2002, **41**,48–76.

[48] P. A. Sigala, E. A. Ruben, C. W. Liu, P. M. B. Piccoli, E. G. Hohenstein, T. J. Martínez, A. J. Schultz and D. Herschlag, *J. Am. Chem. Soc.*, 2015, **137**, 5730–5740.